Electronic Supplementary Information

S-doped AuPd Aerogels as High Efficient Catalysts for Oxygen Reduction Reaction by Balancing the Ratio between bridging S_2^{2-} and apical S^{2-} Ligands

Xiang Zhang,[a] Jing Wang,[c] Mengmeng Zhang,[a] Xinru Yue,[a] Wei Du,[b] Weiliu Fan,[c,*] and Haibing Xia[a,*]

[a] State Key Laboratory of Crystal Materials, Shandong University, Jinan, 250100, P. R. China;

[b] School of Environment and Material Engineering, Yantai University, Yantai, 264005, P. R. China;

[c] School of Chemistry and Chemical Engineering, Shandong University, Jinan, 250100, P. R. China.

*E-mail: hbxia@sdu.edu.cn

Experimental section

Materials.

L-ascorbic acid (AA, 99%) and sodium borohydride ($NaBH_4$, 99%) were purchased from Sinopharm Chemical Reagent Co., Ltd. (Shanghai, China). Reduced glutathione (GSH, 98%) was purchased from Aladdin (Shanghai, China). Sodium tetrachloropalladate(II) hydrate (Na_2PdCl_4, 99%), commercial Pt/C catalysts (nominally 20% on carbon black) and commercial Pd/C catalysts were purchased from Alfa Aesar (Tianjin, China). All the chemicals were used as received without other treatment. All the experiments used Milli-Q water with a resistivity of 18.2 MΩ cm. The aqua regia (3:1 v/v HCl (37%): HNO_3 (65%) solutions) was used for cleaning all glassware thoroughly. And all glassware was washed completely with Milli-Q water before use. (Caution! Aqua regia are dangerous and must be used with extreme care; never store these solutions in closed containers.)

Characterization.

The transmission electron microscopy (TEM) and high-resolution transmission electron microscopy (HRTEM) images of samples were obtained on a JEOL JEM-2100F transmission electron microscope operated at an acceleration voltage of 200 kV. High-angle annular dark-field−scanning transmission electron microscopy (HAADF–STEM) and HAADF–STEM–EDS mapping images were acquired by a JEOL JEM-2100F transmission electron microscope with a STEM unit. The X-ray diffraction (XRD) patterns were obtained on a PANalytical X′pert3 powder diffractometer (40 kV, 40 mA) using a Cu Kα radiation (λ=0.15418 nm). The Raman spectra were recorded by a Renishaw inVia Reflex Raman spectrometer with a 633 nm laser at room temperature. X-ray Photoelectron Spectroscopy (XPS) spectra were recorded by Thermo

Fisher Scientific ESCALAB 250 XPS spectrometer with a monochromatic Al Kα X-ray radiation.

Electrochemical Measurements.

Typically, 0.5 M H_2SO_4 solution has to be deoxygenated by bubbling with high-purity N_2 for at least 30 min before the CO stripping experiments, followed by continuous CO bubbling for 30 min. Then, the CO stripping experiments were performed by holding the electrode potential at 0.03 V (vs Ag/AgCl) in high-purity CO-saturated 0.5 M H_2SO_4 solution with continuous CO bubbling. Next, the electrolyte solution was purged out thoroughly by bubbling with high-purity N_2 for 30 min to guarantee the complete elimination of CO in the electrolyte solution. Eventually, two consecutive CV curves were recorded at the potential range from -0.2 V to 1.1 V (vs Ag/AgCl) at a scan rate of 50 mV s^{-1}.

The electrochemical measurements for ORR were performed in a conventional standard three-electrode system consisting of a saturated calomel electrode (SCE) as the reference electrode, a Pt wire as the counter electrode and rotating disk electrode (RDE) (5 mm in diameter, 0.196 cm^2 in geometric area) as the working electrode. All potentials were transferred to the reversible hydrogen electrode (RHE) on the basis of $E_{RHE} = E_{SCE} + 0.0591 \times pH + 0.241$. The RDE for ORR measurement was polished with 0.05 μm alumina powder carefully, and then washed with Milli-Q water and ethanol under the ultrasonication, followed by drying at room temperature.

The typical prepared procedure for the RDE modified by AuPd-$S_{B_{67}A_{33}}$ aerogels was as follows. The homogenous catalyst ink AuPd-$S_{B_{67}A_{33}}$ aerogels was prepared by ultrasonically dispersing for 30 min at room temperature. Then, about 35 μL of the catalyst ink was dropped

onto the bare RDE, followed by drying in air. Next, 15 μL of an ethanol solution of Nafion (0.2 wt%) was casted onto the surface of the RDE covered with AuPd-$S_{B_{67}A_{33}}$ aerogels, followed by drying in air at room temperature. The mass loading of the catalysts was fixed at 16 μg_{Pd} cm^{-2}.

For comparison, the RDE was also modified by commercial Pt/C catalysts, which was prepared by ultrasonically dispersing 1.23 mg commercial Pt/C catalysts in 1 mL of Milli-Q water containing 0.05 mL of Nafion solution (5 wt%). Then, 20 μL of the commercial Pt/C catalysts ink was dropped onto the bare RDE and dried at room temperature. The Pt loading was fixed at 25 μg_{Pt} cm^{-2}. Similarly, RDEs modified by AuPd-$S_{B_{100}A_0}$ aerogels, AuPd-$S_{B_{50}A_{50}}$ aerogels and commercial Pd/C catalysts were also prepared by the same procedure mentioned above.

The ORR measurements were performed in N_2 and O_2-saturated 0.1 M KOH solutions. Cyclic voltammogram (CV) curves were recorded at cyclic potential range between 0 and 1.4 V (vs RHE) in N_2-saturated 0.1 M KOH solutions at a scan rate of 100 mV s^{-1}. Linear sweep voltammetry (LSV) curves were recorded at 1600 rpm in N_2 and O_2-saturated 0.1 M KOH solutions at a scan rate of 10 mV s^{-1}. The accelerated durability tests (ADTs) were performed in O_2-saturated 0.1 M KOH solutions by applying cyclic potential range between 0.6 and 1.1 V (vs RHE) with a scan rate of 100 mV s^{-1} for 10k, 20k and 30k cycles. Moreover, the chronoamperometric (CA) measurement were employed at 0.7 V (vs RHE) in O_2-saturated 0.1 M KOH solutions at a rotation speed of 1600 rpm for 18000 s.

Fig. S1 LSV curves (A) and histograms (B) of half-wave potentials ($E_{1/2}$) of three types of S-doped AuPd aerogels with different contents of Pb species (a to c) prepared by using the corresponding three types of S-doped AuPb aerogels as templates, which were obtained by three types of network of Au NCs assembled at different concentrations of Pb^{2+} ions. Their LSV curves were all measured at 1600 rpm in O_2-saturated 0.1 M KOH solution. The concentrations of Pb^{2+} ions used for synthesis of these three types of S-doped AuPb aerogels were 1.8 mM (a), 2.0 mM (b) and 2.2 mM (c), respectively. The concentrations of Pd precursor used for synthesis of three types of S-doped AuPd aerogels were all 0.22 mM.

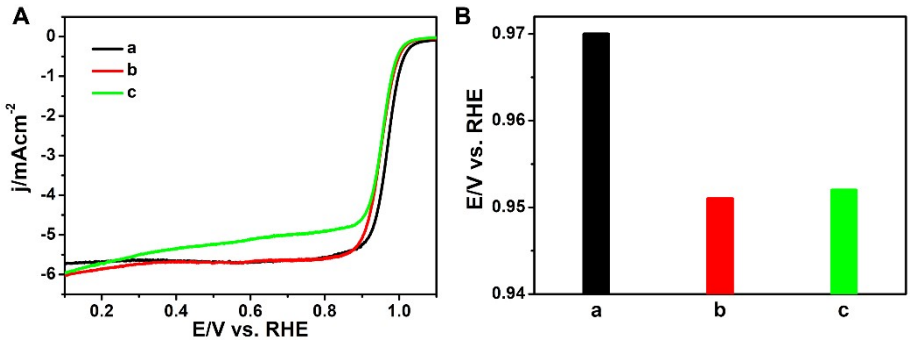

According to the method reported in our previous work,[1] only when the concentration of Pb^{2+} ions is 1.8 mM or above, the Au NCs can self-assemble into the networks of Au NCs. And further increase of the concentration of Pb^{2+} ions above 1.8 mM causes little change in the morphology of the networks of Au NCs and the corresponding S-doped AuPb aerogels derived thereof.

Since PbS and PbS_2 in the S-doped AuPb aerogels are involved with the formation of $Pd_{2.8}S$ and PdS_2 during their conversion into S-doped AuPd aerogels, three types of S-doped AuPb aerogels were firstly prepared by $NaBH_4$ reduction of three types of network of Au NCs assembled at different concentrations of Pb^{2+} ions (1.8 mM, 2.0 mM and 2.2 mM, respectively), which were further used as templates for synthesis of three types of S-doped AuPd aerogels.

The ORR performances of three types of S-doped AuPd aerogels were evaluated by their LSV curves and the corresponding $E_{1/2}$. One can see that with the increasing concentration of Pb^{2+} ions used for preparation of networks of Au NCs from 1.8 to 2.0 and 2.2 mM, the $E_{1/2}$ of three types of S-doped AuPd aerogels are 0.970, 0.951 and 0.952 V, respectively. Therefore, the optimal Pb^{2+} concentration for synthesis of S-doped AuPd aerogels with the optimal electrocatalytic activity is still 1.8 mM.

Fig. S2 LSV curves (A) and histograms (B) of half-wave potentials ($E_{1/2}$) of four types of S-doped AuPd aerogels (a to d). The concentrations of Pd precursors used for synthesis of these four types of S-doped AuPd aerogels are as follows: 0.11 mM (a), 0.16 mM (b), 0.22 mM (c), 0.27 mM (d).

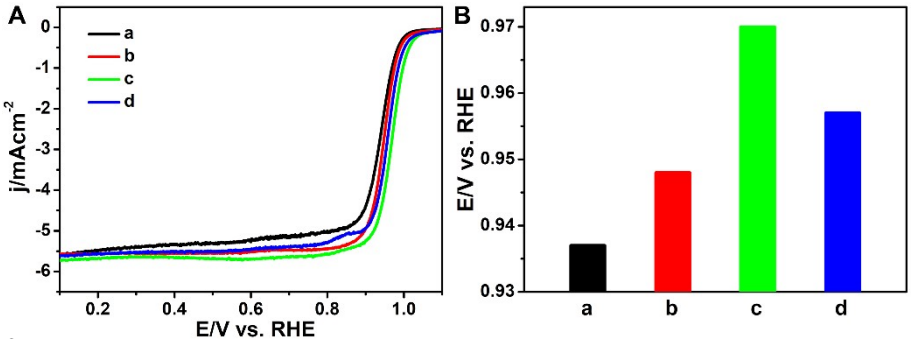

In our case, a series of S-doped AuPd aerogels were synthesized at the fixed concentration of Au precursor by adjusting the concentration of Pd precursors, which were changed from 0.11 to 0.16, 0.22 and 0.27 mM. Accordingly, the corresponding ratio of Pd-to-Au is as follows: 0.05:1, 0.075:1, 0.1:1 and 0.125:1. As shown in Fig. S2, the $E_{1/2}$ values of the S-doped $AuPd_{0.05}$ aerogels, S-doped $AuPd_{0.075}$ aerogels, S-doped $AuPd_{0.10}$ aerogels and S-doped $AuPd_{0.125}$ aerogels were 0.937, 0.948, 0.970 and 0.957 V, respectively, in which the subscript numbers represent the ratio of Pd-to-Au. With the increasing ratio of Pd-to-Au, their $E_{1/2}$ values are firstly increased and then decreased. Thus, the optimal ratio of Pd-to-Au for S-doped AuPd aerogels with an optimal electrocatalytic activity towards to ORR is determined to be 0.1:1. Moreover, the presence of an optimal amount of Au in the as-prepared AuPd-S_{B67A33} aerogels can not only adjust the d-band center of Pd, but also improve their anti-CO poison ability due to the formation of AuPd alloy.

Fig. S3 TEM image of S-doped AuPd aerogels. The concentration of Pd precursor used for synthesis of S-doped AuPd aerogels is 0.27 mM.

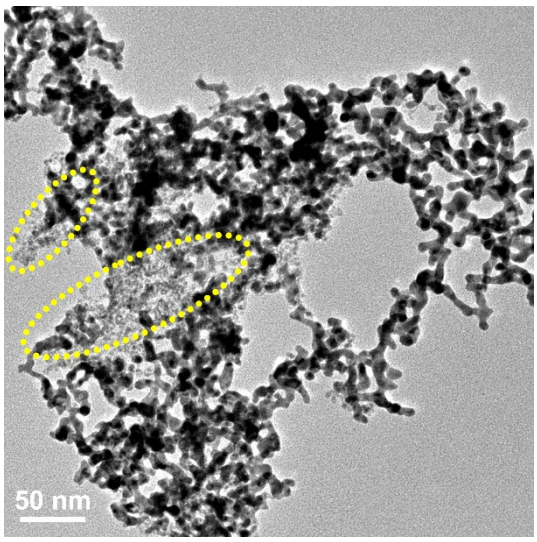

In fact, when the concentration of Pd precursor is as 0.27 mM (Fig. S3), the obtained S-doped AuPd aerogels is nearly same to those obtained with one concentration of Pd precursor below 0.27 mM except the formation of extra Pd nanoparticles (as shown in the highlighted yellow circle). The presence of Pd nanoparticles result in the decrease in their electrocatalytic performance to ORR (d in Fig. S2). Therefore, the optimal concentration of Pd precursors used for synthesis of S-doped AuPd aerogels selected as 0.22 mM. That is the optimal ratio of Pd-to-Au for S-doped AuPd aerogels with an optimal electrocatalytic activity towards to ORR is determined to be 0.1:1.

Fig. S4 Additional TEM images of point defects (yellow circles in a, b and c), line defects (yellow and red lines in c, d and e), plane defects (yellow and cyan lines in b and d) and deformation twinning (wave-like yellow, cyan and red lines in c and e to h) existed in in the as-prepared AuPd-$S_{B_{67}A_{33}}$ aerogels.

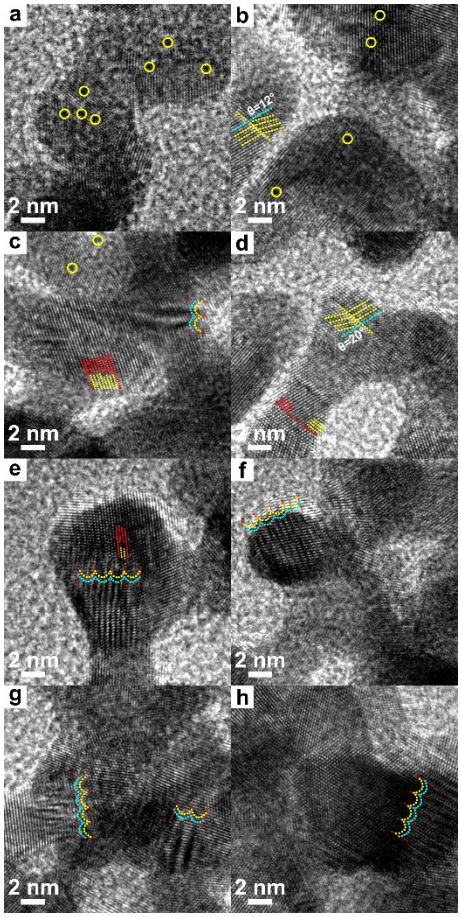

Fig. S5 CV curve of AuPd-$S_{B_{67}A_{33}}$ aerogels measured in N_2-saturated 0.1 M KOH solution with a scan rate of 100 mV s^{-1}.

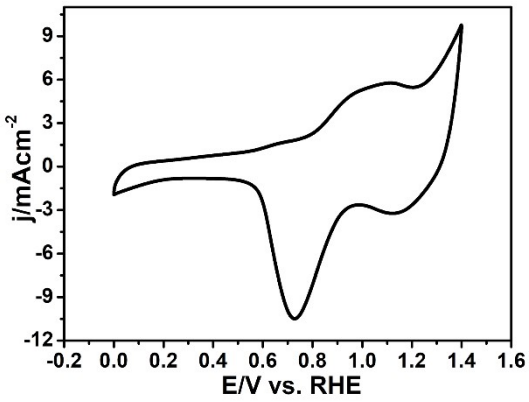

As shown in Fig. S5, the AuPd-$S_{B_{67}A_{33}}$ aerogels exhibit the obvious characteristic peaks of Pd (at about 0.728 V vs. RHE) and Au (at about 1.123 V vs. RHE) in 0.1 M KOH solution. The result indicates that both elemental Pd and Au exist on the surfaces of the AuPd-$S_{B_{67}A_{33}}$ aerogels.

Fig. S6 XRD patterns of three types of AuPd-$S_{B_xA_y}$ aerogels: AuPd-$S_{B_{100}A_0}$ aerogels (a, black curve), AuPd-$S_{B_{67}A_{33}}$ aerogels (b, red curve) and AuPd-$S_{B_{50}A_{50}}$ aerogels (c, dark yellow curve), which were obtained by the three types of S-doped AuPb aerogels as templates via the reduction of the same type of network of Au NCs connected by Pb^{2+} ions with an insufficient amount of $NaBH_4$ (a), with a proper amount of $NaBH_4$ (b) and with an excessive amount of $NaBH_4$ (c), respectively. For better comparison, the signal intensities in these XRD patterns are normalized by the signal intensity of pure Au (JCPDS No.04-0708) at 37.9°.

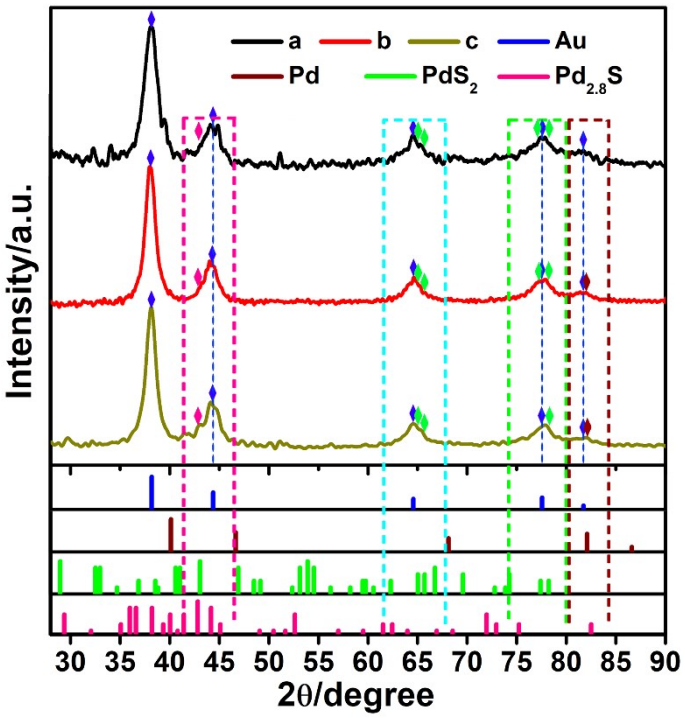

In order to identify the main constituent of the AuPd-$S_{B_{67}A_{33}}$ aerogels, the XRD patterns of other two types of AuPd-$S_{B_xA_y}$ aerogels (AuPd-$S_{B_{100}A_0}$ aerogels and AuPd-$S_{B_{50}A_{50}}$ aerogels) were also investigated by X-ray diffraction and compared with that of AuPd-$S_{B_{67}A_{33}}$ aerogels. As shown in Fig.S6, the main diffraction peaks of AuPd-$S_{B_{100}A_0}$ aerogels (black curve), AuPd-$S_{B_{67}A_{33}}$ aerogels (red curve) and AuPd-$S_{B_{50}A_{50}}$ aerogels (dark yellow curve) are located at about 37.9°, 44.0°, 64.6°, 78.0° and 81.9° (blue rhombus), which are basically consistent with those of the pure Au (JCPDS No.04-0708) due to the high Au content in the three types of AuPd-$S_{B_xA_y}$ aerogels (78.10 % in AuPd-$S_{B_{100}A_0}$ aerogels, 82.16 % in AuPd-$S_{B_{67}A_{33}}$ aerogels and 82.44 % in AuPd-$S_{B_{50}A_{50}}$ aerogels, Table S4).

The diffraction peaks at the range of 41.5° to 46.5° (within the pink dotted rectangle) can be mainly assigned to $Pd_{2.8}S$ (pink rhombus, JCPDS No.10-0334), PdS_2 (green rhombus, JCPDS No.11-0497) and Au (blue rhombus, JCPDS No.04-0708). Compared with AuPd-$S_{B_{100}A_0}$ aerogels and AuPd-$S_{B_{67}A_{33}}$ aerogels, the AuPd-$S_{B_{50}A_{50}}$ aerogels show one obvious shoulder peak at 43.0° (pink rhombus) on the left-side of this main diffraction peak, which can be assigned to $Pd_{2.8}S$ (JCPDS No.10-0334), instead of PdS_2 (JCPDS No.11-0497). This is because the content of PbS in the corresponding S-doped AuPb aerogels used for synthesis of the AuPd-$S_{B_{50}A_{50}}$ aerogels is obviously higher than that in the corresponding S-doped AuPb aerogels used for synthesis of the AuPd-$S_{B_{100}A_0}$ aerogels and AuPd-$S_{B_{67}A_{33}}$ aerogel (Fig.S7). Accordingly, $Pd_{2.8}S$ may be the main compound exist in the AuPd-$S_{B_{50}A_{50}}$ aerogels while PdS_2 may be the

main compound exist in the AuPd-$S_{B_{100}A_0}$ aerogels as well as AuPd-$S_{B_{67}A_{33}}$ aerogel due to the presence of higher content of bridging S_2^{2-} ligands demonstrated by their XPS and Raman results (Fig. 6 and 8).

In contrast, the diffraction peaks at the range of 73.9° to 79.6° (within the green dotted rectangle) can be mainly assigned to PdS_2 (green rhombus, JCPDS No.11-0497) and Au (blue rhombus, JCPDS No.04-0708) as well as $Pd_{2.8}S$ (pink rhombus, JCPDS No.10-0334). In contrast, the top parts of diffraction peaks at the range of 73.9° to 79.6° of the AuPd-$S_{B_{100}A_0}$ aerogels and AuPd-$S_{B_{67}A_{33}}$ aerogels looks like flat while that of AuPd-$S_{B_{50}A_{50}}$ aerogels is sharp. In addition, the FWHMs of the diffraction peaks at the range of 73.9° to 79.6° of the AuPd-$S_{B_{100}A_0}$ aerogels and AuPd-$S_{B_{67}A_{33}}$ aerogels are bigger than that of AuPd-$S_{B_{50}A_{50}}$ aerogels. This is because of the presence of two diffraction peaks (around 77.4° and 78.2°) on their left and right sides of diffraction peaks at the range of 73.9° to 79.6°. The results indicate that the order of content of PdS_2 in the AuPd-$S_{B_{100}A_0}$ aerogels, AuPd-$S_{B_{67}A_{33}}$ aerogels and AuPd-$S_{B_{50}A_{50}}$ aerogels is as follow: AuPd-$S_{B_{100}A_0}$ aerogels > AuPd-$S_{B_{67}A_{33}}$ aerogels > AuPd-$S_{B_{50}A_{50}}$ aerogels. This is because the contents of PbS_2 in the corresponding S-doped AuPb aerogels used for synthesis of the AuPd-$S_{B_{100}A_0}$ aerogels, AuPd-$S_{B_{67}A_{33}}$ aerogels and AuPd-$S_{B_{50}A_{50}}$ aerogels gradually decrease (Fig.S7). Accordingly, PdS_2 (JCPDS No.11-0497) may be the main compound exist in the AuPd-$S_{B_{100}A_0}$ aerogels and AuPd-$S_{B_{67}A_{33}}$ aerogel due to the presence of higher content of bridging S_2^{2-} ligands demonstrated by their XPS and Raman results (Fig. 6 and 8) while $Pd_{2.8}S$ may be the main compound exist in the AuPd-$S_{B_{50}A_{50}}$ aerogels mentioned above.

Meanwhile, the order of the FWHMs of the diffraction peaks at the range of 61.5° to 67.9° (within the cyan dotted rectangle) of the AuPd-$S_{B_{100}A_0}$ aerogels, AuPd-$S_{B_{67}A_{33}}$ aerogels and AuPd-$S_{B_{50}A_{50}}$ aerogels is as follow: AuPd-$S_{B_{100}A_0}$ aerogels > AuPd-$S_{B_{67}A_{33}}$ aerogels > AuPd-$S_{B_{50}A_{50}}$ aerogels. The results also indicate the contents of PdS_2 (around 65.0° and 65.7°JCPDS No.11-0497) in AuPd-$S_{B_{100}A_0}$ aerogels, AuPd-$S_{B_{67}A_{33}}$ aerogels and AuPd-$S_{B_{50}A_{50}}$ aerogels gradually decrease. And this is due to the same reason that the contents of PbS_2 in the corresponding S-doped AuPb aerogels used for synthesis of the AuPd-$S_{B_{50}A_{50}}$ aerogels gradually decrease (Fig.S7).

The diffraction peaks centered at about 82.0° (wine rhombus, within the wine dotted rectangle) in the XRD patterns can be assigned to Pd (JCPDS No.46-1043). In contrast, there are visible peaks in the AuPd-$S_{B_{67}A_{33}}$ aerogels and AuPd-$S_{B_{50}A_{50}}$ aerogels while there is no any visible peak in AuPd-$S_{B_{100}A_0}$ aerogels. The results mean that a certain amount of Pd(0) atoms exist in the AuPd-$S_{B_{67}A_{33}}$ aerogels and AuPd-$S_{B_{50}A_{50}}$ aerogels while the content of Pd(0) atoms in AuPd-$S_{B_{100}A_0}$ aerogels is rather low. In addition, due to the presence of the low content of Pd(0) atoms, there are no other visible diffraction peaks of Pd observed in XRD patterns of AuPd-$S_{B_{67}A_{33}}$ aerogels and AuPd-$S_{B_{50}A_{50}}$ aerogels.

Fig.S7 XRD patterns of three types of S-doped AuPb aerogels contained with different amount of S species (a, b and c), which were obtained by the reduction of the same network of Au NCs connected by Pb^{2+} ions with an insufficient amount of $NaBH_4$ (a, black curve), with a proper amount of $NaBH_4$ (b, red curve) and with an excessive amount of $NaBH_4$ (c, dark yellow curve), respectively. Note that three types of S-doped AuPb aerogels with different amount of S species were used to further prepare AuPd-$S_{B_{100}A_0}$ aerogels, AuPd-$S_{B_{67}A_{33}}$ aerogels and AuPd-$S_{B_{50}A_{50}}$ aerogels, respectively (samples in Fig.S6).

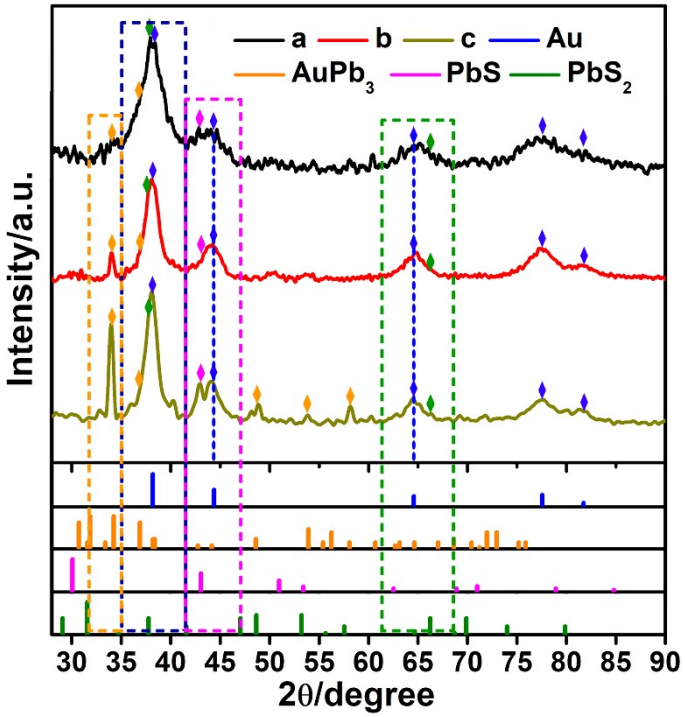

As shown in Fig.S7, the XRD patterns of the S-doped AuPb aerogels obtained by the reduction of the same network of Au NCs connected by Pb^{2+} ions with an insufficient amount of $NaBH_4$ (a, black curve, denote as AuPb-1 aerogels), a proper amount of $NaBH_4$ (b, red curve, denote as AuPb-2 aerogels) and an excessive amount of $NaBH_4$ (c, dark yellow curve, denote as AuPb-3 aerogels) were investigated by X-ray diffraction. The main diffraction peaks of AuPb-1 aerogels, AuPb-2 aerogels and AuPb-3 aerogels are located at about 38.1°, 44.2°, 64.8°, 77.7° and 81.9° (blue rhombus), which are basically consistent with those of the pure Au (JCPDS No.04-0708) due to the high Au content in the three types of S-doped AuPb aerogels (80.40 % in AuPb-1 aerogels, 88.48 % in AuPb-2 aerogels and 92.41 % in AuPb-3 aerogels).

The diffraction peaks at the range of 34.8° to 41.5° (within the navy dotted rectangle) can be mainly assigned to Au (blue rhombus, 38.1°), $AuPb_3$ (orange rhombus, 36.9°) and PbS_2 (olive rhombus, 37.9°). One can clearly see that the FWHMs of the AuPb-1 aerogels, AuPb-2 aerogels and AuPb-3 aerogels decrease gradually. In the range of 34.8° to 41.5° (within the navy dotted rectangle) of the XRD patterns of AuPb-1 aerogels, larger FWHM of the peak centered around 38.1° in the AuPb-1 aerogels is possibly due to the presence of the diffraction peaks at 37.9° (olive rhombus) on its left-side, which are assigned to PbS_2 (JCPDS No.20-0596). In contrast, there are no obvious diffraction peak at 37.9°on the left-side of the peak centered around 38.1° in the AuPb-2 aerogels and AuPb-3 aerogels. And the FWHMs of AuPb-2 aerogels and AuPb-3 aerogels decrease gradually. These results indicate that the order of the content of PbS_2 in the

AuPb-1 aerogels, AuPb-2 aerogels and AuPb-3 aerogels is as follows: AuPb-1 aerogels > AuPb-2 aerogels > AuPb-3 aerogels.

Moreover, the diffraction peak at the range of 61.4° to 68.3° (within the olive dotted rectangle) also can be assigned to PbS_2 (olive rhombus, 66.3°) and Au (blue rhombus, 64.6°). It can be clearly seen that the FWHMs of the peaks centered around 64.8° in the AuPb-1 aerogels, AuPb-2 aerogels and AuPb-3 aerogels decrease gradually. The broadening in their FWHMs is possibly due to the presence of should peaks on their right-side, which are attributed to the PbS_2 (around 66.3°). In view of the broadening in their FWHMs, the content of PbS_2 in the AuPb-1 aerogels, AuPb-2 aerogels and AuPb-3 aerogels also follows the same order: AuPb-1 aerogels > AuPb-2 aerogels > AuPb-3 aerogels. Accordingly, the order of the content of PdS_2 in the AuPd-$S_{B_{100}A_0}$ aerogels, AuPd-$S_{B_{67}A_{33}}$ aerogels and AuPd-$S_{B_{50}A_{50}}$ aerogels is as follows: AuPd-$S_{B_{100}A_0}$ aerogels > AuPd-$S_{B_{67}A_{33}}$ aerogels > AuPd-$S_{B_{50}A_{50}}$ aerogels because PbS_2 would transform into PdS_2 during their synthesis.

The diffraction peaks at 34.0° (orange rhombus) can be assigned to $AuPb_3$ (JCPDS No.26-0711). Their intensities in the XRD patterns of the AuPb-1 aerogels, AuPb-2 aerogels and AuPb-3 aerogels increase gradually, indicating the contents of $AuPb_3$ in them gradually increases. In addition, those diffraction peak at 48.8°, 53.8° and 58.2° also belong to $AuPb_3$, which were more obvious in AuPb-3 aerogels than those in the AuPb-1 aerogels and AuPb-2 aerogels, indicating that the order of the content of $AuPb_3$ in the AuPb-1 aerogels, AuPb-2 aerogels and AuPb-3 aerogels is as follows: AuPb-3 aerogels > AuPb-2 aerogels > AuPb-1 aerogels. Accordingly, the content of AuPd in AuPd-$S_{B_{50}A_{50}}$ aerogels is higher than those in the AuPd-$S_{B_{100}A_0}$ aerogels and AuPd-$S_{B_{67}A_{33}}$ aerogels because $AuPb_3$ would transform into AuPd during their synthesis. Consequently, the order of the content of AuPd in the AuPd-$S_{B_{100}A_0}$ aerogels, AuPd-$S_{B_{67}A_{33}}$ aerogels and AuPd-$S_{B_{50}A_{50}}$ aerogels is as follows: AuPd-$S_{B_{100}A_0}$ aerogels < AuPd-$S_{B_{67}A_{33}}$ aerogels < AuPd-$S_{B_{50}A_{50}}$ aerogels.

The diffraction peaks at the range of 41.4° to 46.9° (within the magenta dotted rectangle) can be mainly assigned to PbS (magenta rhombus, 42.9°) and Au (blue rhombus, 44.2°). And the diffraction peak at about 42.9° (magenta rhombus) belongs to PbS (JCPDS No.05-0592). The AuPb-3 aerogels exhibit a very obvious diffraction peak of PbS (magenta rhombus) on the left-side of the diffraction peak centered at about 44.2° while there is no any obvious diffraction peak on the left-side of the same peaks in the AuPb-1 aerogels and AuPb-2 aerogels. The results suggest that the content of PbS in AuPb-3 aerogels is higher than that of AuPb-1 aerogels and AuPb-2 aerogels. And the FWHMs of the AuPb-1 aerogels and AuPb-2 aerogels and AuPb-3 aerogels increase gradually due to the increasing content of PbS in them. That is, the order of the content of PbS in the AuPb-1 aerogels and AuPb-2 aerogels and AuPb-3 aerogels is as follows: AuPb-1 aerogels < AuPb-2 aerogels < AuPb-3 aerogels. Accordingly, the content of $Pd_{2.8}S$ in AuPd-$S_{B_{50}A_{50}}$ aerogels is higher than those in the AuPd-$S_{B_{100}A_0}$ aerogels and AuPd-$S_{B_{67}A_{33}}$ aerogels because PbS would transform into $Pd_{2.8}S$ during their synthesis. Consequently, the order of the content of $Pd_{2.8}S$ in the AuPd-$S_{B_{100}A_0}$ aerogels, AuPd-$S_{B_{67}A_{33}}$ aerogels and AuPd-$S_{B_{50}A_{50}}$ aerogels is as follows: AuPd-$S_{B_{100}A_0}$ aerogels < AuPd-$S_{B_{67}A_{33}}$ aerogels < AuPd-$S_{B_{50}A_{50}}$ aerogels.

On the basis of results mentioned above (Fig.S6 and S7), the contents of PdS_2 and $Pd_{2.8}S$ in AuPd-$S_{B_{67}A_{33}}$ aerogels are well balanced, compared with AuPd-$S_{B_{100}A_0}$ aerogels and AuPd-

$S_{B_{50}A_{50}}$ aerogels, which have higher contents of PdS_2 and $Pd_{2.8}S$, respectively. In addition, the content of AuPd in the AuPd-$S_{B_{100}A_0}$ aerogels, AuPd-$S_{B_{67}A_{33}}$ aerogels and AuPd-$S_{B_{50}A_{50}}$ aerogels gradually increase.

Fig. S8 Raman spectra of GSH molecules (a), Au NCs (b), network of Au NCs connected by Pb^{2+} ions (c), S-doped AuPb aerogels (d) and AuPd-$S_{B_{67}A_{33}}$ aerogels (e). Note that their Raman spectra at a range of 2100-2900 cm^{-1} were selectively shown for better comparison.

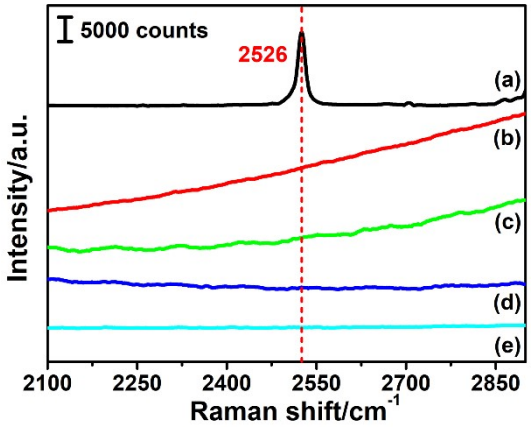

The Raman spectra of GSH molecules, Au NCs, the network of Au NCs connected by Pb^{2+} ions, S-doped AuPb aerogels and AuPd-$S_{B_{67}A_{33}}$ aerogels in the range of 2100-2900 cm^{-1} compared. As shown in Fig. S9a, the Raman signal located at about 2526 cm^{-1} is assigned to the characteristic peak of S–H bonds of the GSH molecules, which was used for preparation of Au NCs.[2-4] During the synthesis of Au NCs with the GSH, the S–H bonds in GSH would transform into the bridging S–S bonds.[2-4] Accordingly, the Raman signal at 2526 cm^{-1} in Au NCs (Fig. S8b, red curve) is absent. So do the network of Au NCs connected by Pb^{2+} ions, S-doped AuPb aerogels and AuPd-$S_{B_{67}A_{33}}$ aerogels. Thus, bridging S–S bonds are present in network of Au NCs connected by Pb^{2+} ions, S-doped AuPb aerogels and AuPd-$S_{B_{67}A_{33}}$ aerogels.

Fig. S9 XPS spectra of Au 4f signals of pure Au NPs (A), AuPd-$S_{B_{100}A_0}$ aerogels (B), AuPd-$S_{B_{67}A_{33}}$ aerogels (C) and AuPd-$S_{B_{50}A_{50}}$ aerogels (D).

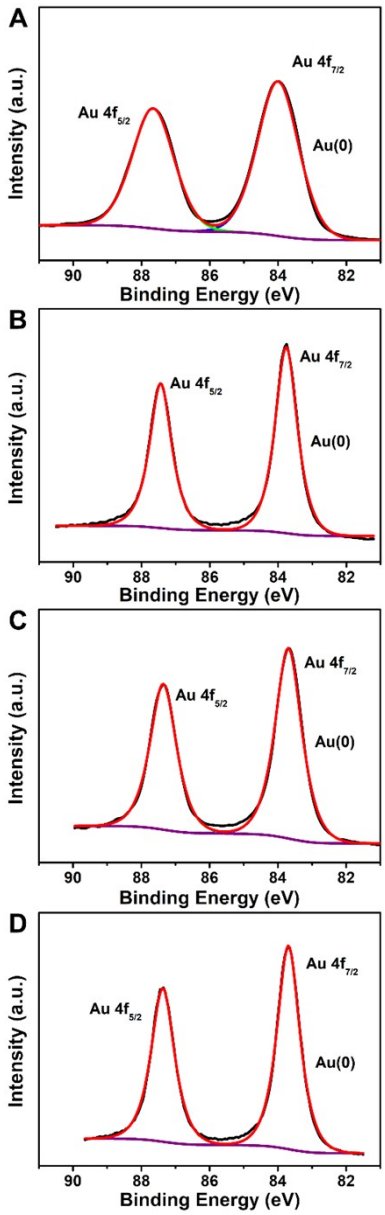

As shown in Fig. S9, the binding energies (BEs) of Au $4f_{7/2}$ and Au $4f_{5/2}$ signals of pure Au NPs (Fig. S9A), the AuPd-$S_{B_{100}A_0}$ aerogels (Fig. S9B), the AuPd-$S_{B_{67}A_{33}}$ aerogels (Fig. S9C) and the AuPd-$S_{B_{50}A_{50}}$ aerogels (Fig. S9D) are 84.0 eV and 87.7 eV (Fig. S9A), 83.8 eV and 87.5 eV (Fig. S9B), 83.7 eV and 87.4 eV (Fig. S9C), 83.7 eV and 87.4 eV (Fig. S9D), respectively.

Fig. S10 XPS spectrum of the O 1s signals of the AuPd-$S_{B_{67}A_{33}}$ aerogels.

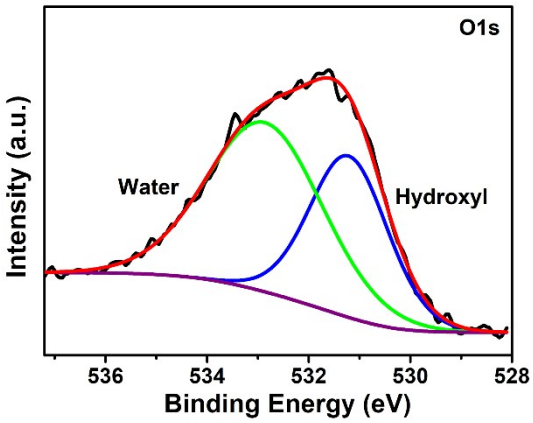

As shown in Fig. S10, the main BEs of O 1s signal of the AuPd-$S_{B_{67}A_{33}}$ aerogels are about 531.3 and 533.0 eV, which could be ascribed to the surface hydroxyl groups and adsorbed water,[5,6] respectively, instead of the lattice oxygen.

Fig. S11 LSV curves (A) and histograms (B) of half-wave potentials ($E_{1/2}$) of S_m-doped AuPd aerogels obtained by using the different types of S-doped AuPb aerogels, which were obtained by reduction of Au NCs via different amounts of $NaBH_4$, in which m represents the volume of $NaBH_4$ (0.10 M): 50 μL (a), 100 μL (b), 150 μL (c), 200 μL (d). These LSV curves were measured in O_2-saturated 0.1 M KOH solution at 1600 rpm. The concentrations of Pd precursor used for synthesis S-doped AuPd aerogels were all 0.22 mM.

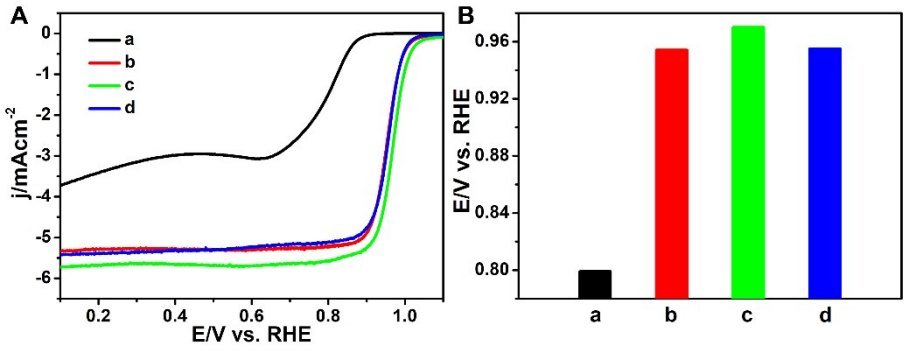

Fig. S12 EDS spectra of AuPd-S_{B67A33} aerogels (A), AuPd-S_{B50A50} aerogels (B) and S-doped AuPd aerogels (C) obtained by a higher amount of $NaBH_4$ (three times more).

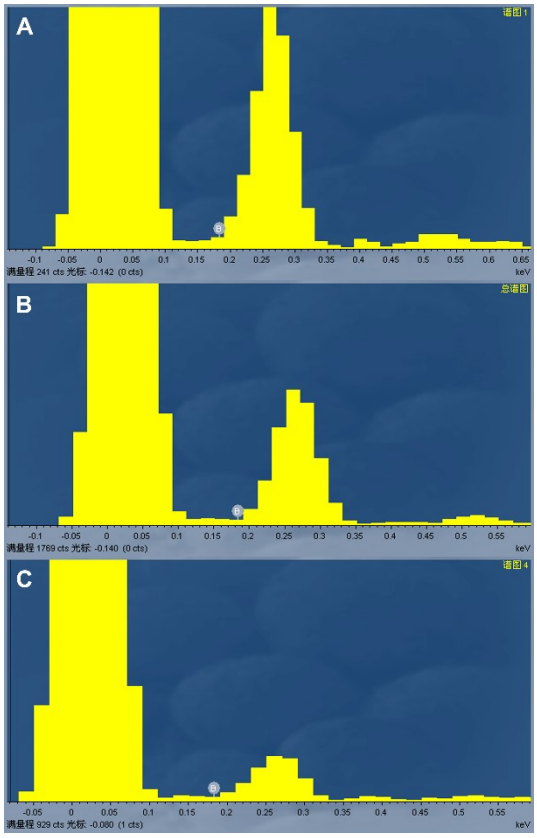

When $NaBH_4$ is used as reducing agents at room temperature for synthesis, there is hardly any literature reported that elemental B can be introduced into the catalysts, especially in Pd or Pt-based catalysts.[7-11] On the basis of EDS results, there is hardly any signal of elemental B observed in the EDS spectra of AuPd-S_{B67A33} aerogels and AuPd-S_{B50A50} aerogels (Fig.S12 A and B). Moreover, even when a higher amount of $NaBH_4$ (three times more) used for synthesis of S-doped AuPb aerogels, there is still no any signal of elemental B observed in the EDS spectrum (Fig. S12C). Furthermore, the signal of elemental B in these three EDS spectra are nearly the same. These results indicate that the weak signal of elemental B is background noise, instead of its real signal. Thus, elemental B cannot be introduced in the resulting catalysts by $NaBH_4$ reduction at room temperature. Moreover, elemental B is generally introduced by boric acid[12-15] or BCl_3[16-18] as B source. In brief, elemental B is not introduced into the as-prepared catalysts when $NaBH_4$ is used as reducing agents at room temperature for synthesis of Pd or Pt-based catalysts.

Fig. S13 CV curves (A, C and E) and LSV curves (B, D and F) of commercial Pd/C catalysts (A and B), AuPd-$S_{B_{100}A_0}$ aerogels (C and D) and AuPd-$S_{B_{50}A_{50}}$ aerogels (E and F), which were measured in N_2 (A, C and E) and O_2 (B, D and F) saturated 0.1 M KOH solution, respectively.

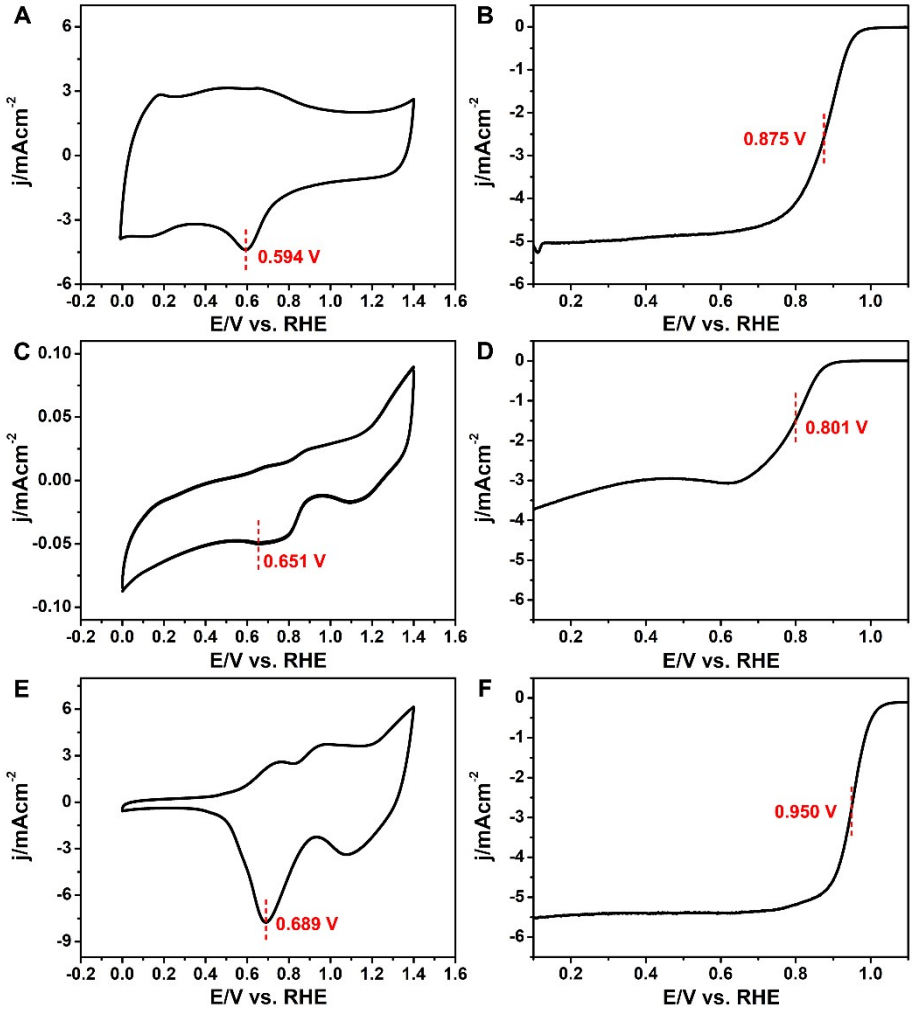

Fig. S14 Koutecky-Levich (K-L) plots of AuPd-$S_{B_{50}A_{50}}$ aerogels (A) and commercial Pt/C catalysts (B) within the potential range from 0.5 to 0.7 V (vs RHE).

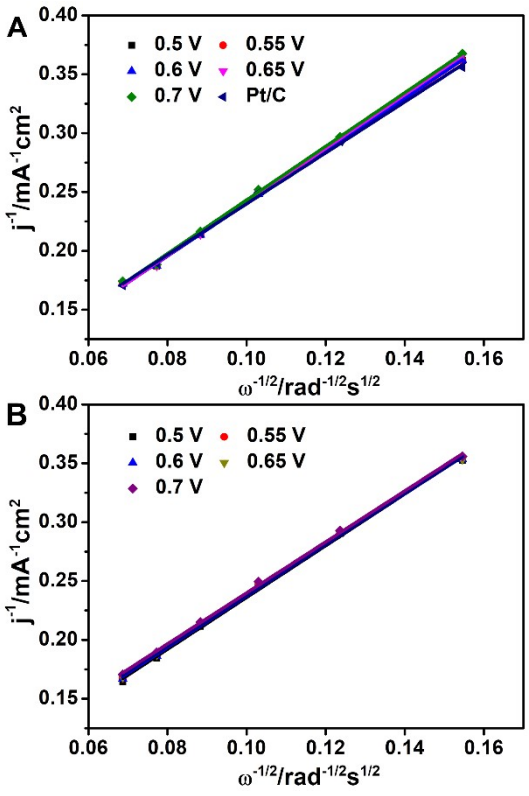

Fig. S15 LSV curves of AuPd-$S_{B_{67}A_{33}}$ aerogels (A), AuPd-$S_{B_{50}A_{50}}$ aerogels (B) and commercial Pt/C catalysts (C), which were measured in O_2-saturated 0.1 M KOH solution at a scan rate of 10 mV s^{-1} over a range of rotation speed from 400 to 2025 rpm.

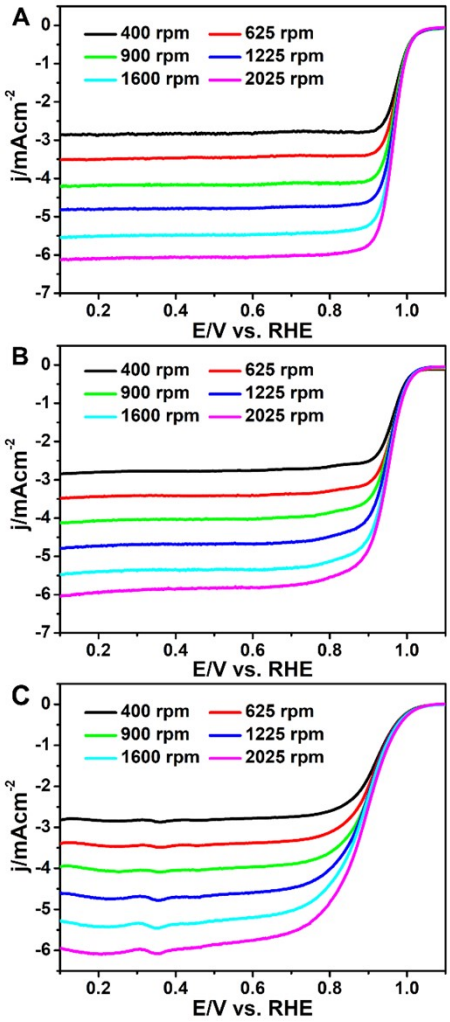

The number of electrons transferred (n) and kinetic current density (j_k) are obtained from the Koutecky-Levich equation:[19-21]

$$\frac{1}{j} = \frac{1}{j_k} + \frac{1}{j_d} = \frac{1}{j_k} + \frac{1}{B\omega^{1/2}}$$

$$B = 0.62nFC_0D_0^{2/3}\nu^{-1/6}$$

where j is the measured current density, j_k is the kinetic current density, and j_d is the diffusion limiting current density. ω is the angular velocity of the disk ($\omega = 2\pi N$, N is the linear rotation speed); n is the overall number of electrons transferred in the whole reaction; F is Faraday constant (F = 96485 C mol^{-1}); C_0 is the bulk concentration of dissolved oxygen (1.2×10^{-6} mol cm^{-3} in 0.1 M KOH solution); D_0 is the diffusion coefficient of dissolved oxygen (1.9×10^{-5} cm^2 s^{-1} in 0.1 M KOH solution); ν is the kinematic viscosity of the electrolyte (0.01 cm^2 s^{-1} for 0.1 M KOH solution).[22-24]

Fig. S16 The electron transfer number at different potentials of AuPd-$S_{B_{67}A_{33}}$ aerogels (a), AuPd-$S_{B_{50}A_{50}}$ aerogels (b) and commercial Pt/C catalysts (c).

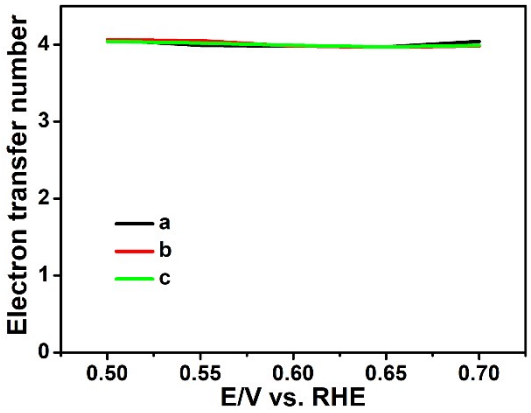

Fig. S17 Tafel plots of commercial Pt/C catalysts (black) and AuPd-$S_{B_{50}A_{50}}$ aerogels (red).

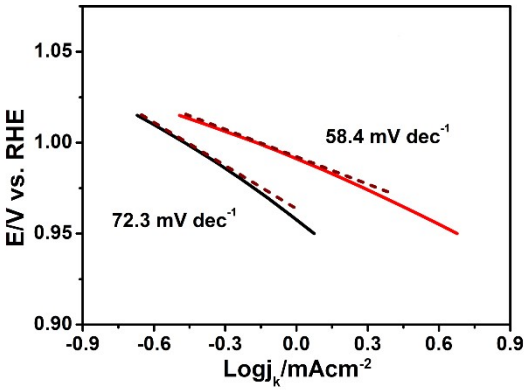

Fig. S18 Histograms of kinetic current density of commercial Pt/C catalysts (a, black color), AuPd-$S_{B_{50}A_{50}}$ aerogels (b, red color) and AuPd-$S_{B_{67}A_{33}}$ aerogels (c, green color) at 0.9 V vs. RHE.

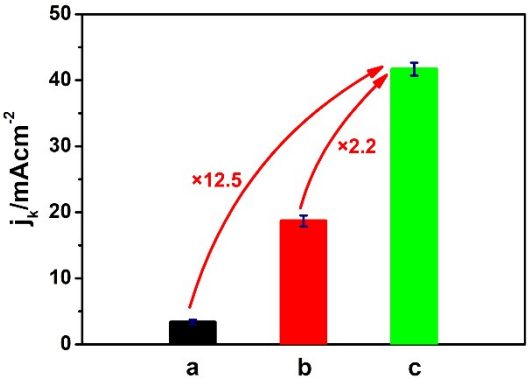

Fig. S19 CO stripping voltammograms of AuPd-$S_{B_{50}A_{50}}$ aerogels (A) and commercial Pt/C catalysts (B), which were measured in 0.5 M H_2SO_4 solution at a scan rate of 50 mV s^{-1}.

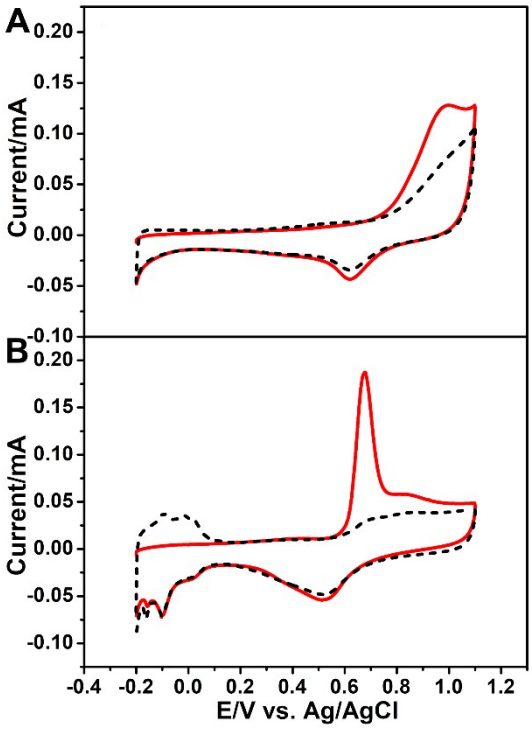

The electrochemically active surface areas (ECSA) of the samples are calculated based on the equation:[25,26]

$$ECSA = \frac{Q}{mC}$$

where Q is the charge in the CO adsorption region, m was the Pd loading on the electrode, and C was the charge required for monolayer adsorption of CO on Pd surface (420 μC cm^{-2}).[27,28]

Fig. S20 Histograms of mass activity and specific activity of commercial Pt/C catalysts (black color) and AuPd-$S_{B_{50}A_{50}}$ aerogels (red color) at 0.9 V vs. RHE.

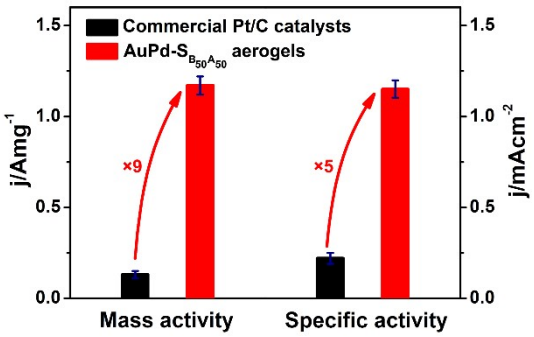

Fig. S21 LSV curves of the as-prepared AuPd-S_{B67A33} aerogels in O_2-saturated 0.1 M $HClO_4$ solution (a, black curve), 0.1 M PBS (b, red curve) and 0.1 M KOH solution (c, green curve) at 1600 rpm.

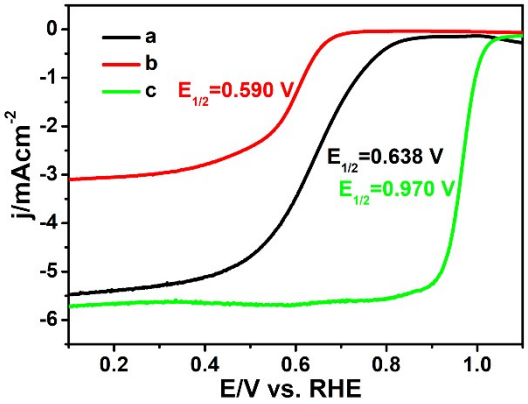

The ORR activities in the neutral and acidic media were further investigated by LSV curves, respectively. For better comparison, the LSV curves of the as-prepared AuPd-S_{B67A33} aerogels in the acid, neutral and alkaline media are all shown in Fig. S21. It is clearly seen that the $E_{1/2}$ of the as-prepared AuPd-S_{B67A33} aerogels in O_2-saturated 0.1 M $HClO_4$ solution, 0.1 M PBS and 0.1 M KOH solution are 0.638 V, 0.590 V and 0.970 V, respectively. Moreover, compared with their excellent ORR activity in alkaline media, the ORR activity of the as-prepared AuPd-S_{B67A33} aerogels in acid and neutral media are worse than and comparable to that of commercial Pt/C catalysts in literatures,[29] respectively.

Fig. S22 TEM image (a), HAADF–STEM image (b), HAADF–STEM–EDS mapping images (c, d and e) and HAADF–STEM–EDS spectrum (f) of the as-prepared S-doped AuPb aerogels. The elements in (c), (d), and (e) are Au (red), Pb (green), and S (yellow), respectively.

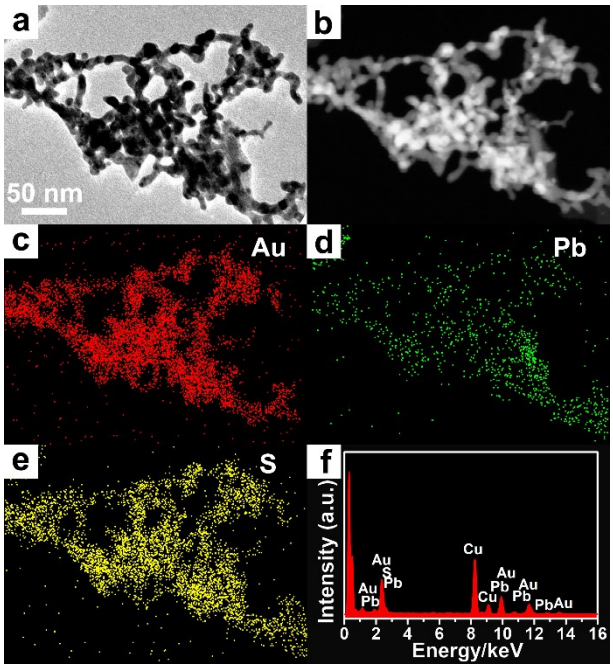

Fig. S23 TEM image (a), HAADF–STEM image (b), HAADF–STEM–EDS mapping images (c and d) and HAADF–STEM–EDS spectrum (e) of the as-prepared AuPd aerogels. The elements in (c) and (d) are Au (red) and Pd (yellow), respectively.

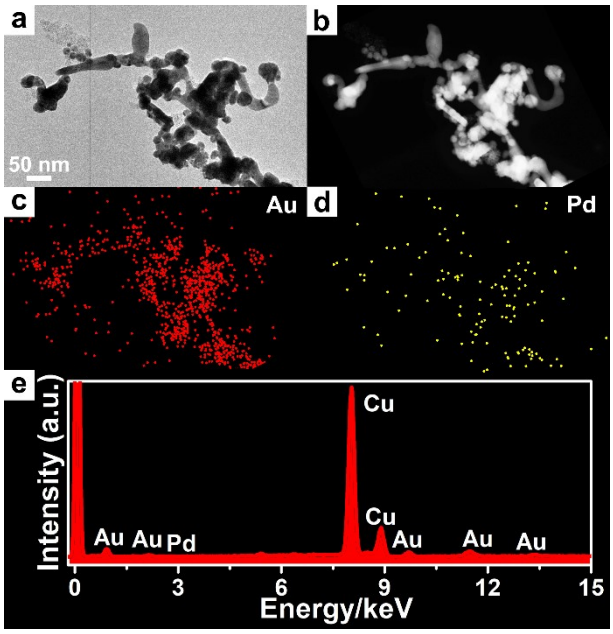

Fig. S24 LSV curves of the as-prepared AuPd-S_{B67A33} aerogels (a, black curve) and S-doped AuPb aerogels (b, red curve), measured in O_2-saturated 0.1 M KOH solution.

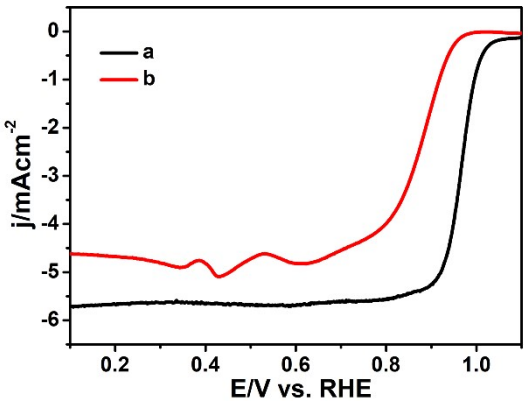

Fig. S25 LSV curves of the as-prepared AuPd-S_{B67A33} aerogels (a, black curve) and AuPd aerogels (b, red curve), measured in O_2-saturated 0.1 M KOH solution.

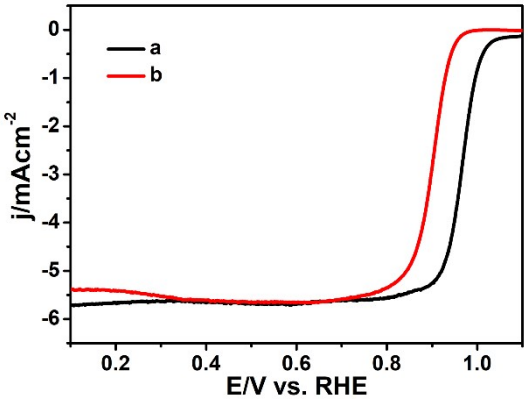

Fig. S26 TEM image (a), HAADF–STEM image (b), HAADF–STEM–EDS mapping images (c and d) and HAADF–STEM–EDS spectrum (e) of the as-prepared Pd-S catalysts. The elements in (c) and (d) are Pd (red) and S (green), respectively.

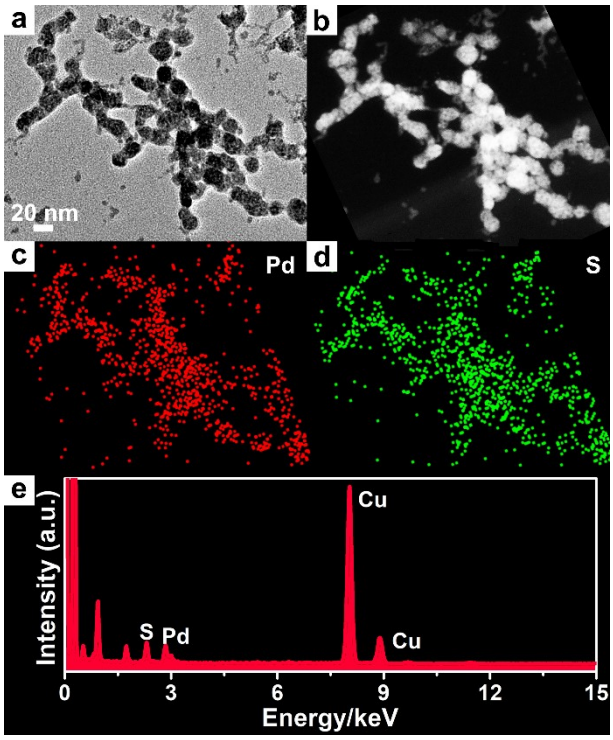

Fig. S27 LSV curves of the as-prepared AuPd-S_{B67A33} aerogels (a, black curve), Pd-S catalysts (b, red curve) and commercial Pd/C catalysts (c, green curve) in O_2-saturated 0.1 M KOH solution at 1600 rpm.

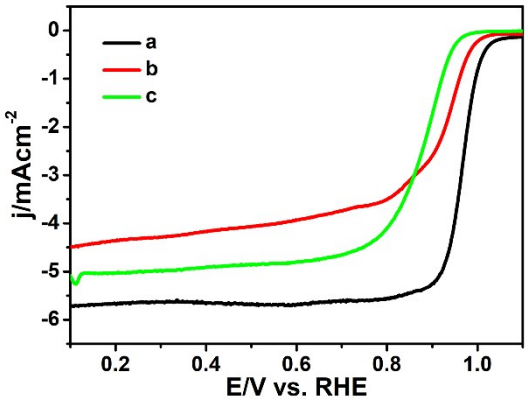

Fig. S28 LSV curves of AuPd-$S_{B_{50}A_{50}}$ aerogels before and after ADTs of 10k, 20k and 30k cycles between 0.6 and 1.1 V (vs RHE) at scan rate of 100 mV s^{-1} in 0.1 M KOH solution.

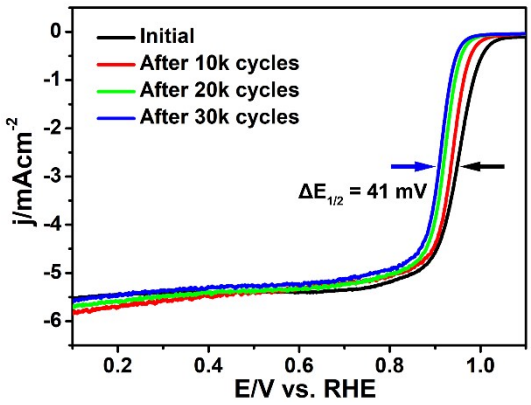

Fig. S29 LSV curves of commercial Pt/C catalysts before and after ADTs of 10k, 20k and 30k cycles between 0.6 and 1.1 V (vs RHE) at scan rate of 100 mV s^{-1} in 0.1 M KOH solution.

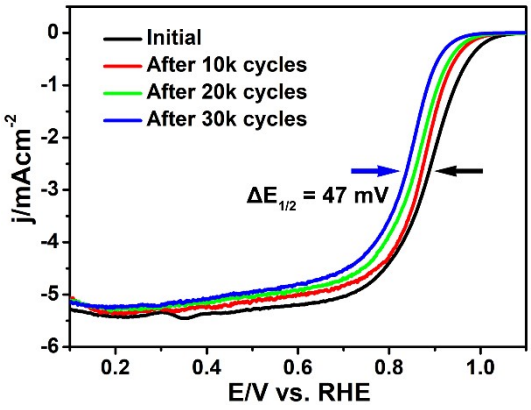

Fig. S30 HAADF–STEM image (a), HAADF–STEM–EDS mapping images (b to d) of the as-prepared AuPd-S_{B67A33} aerogels after the ADT testing.

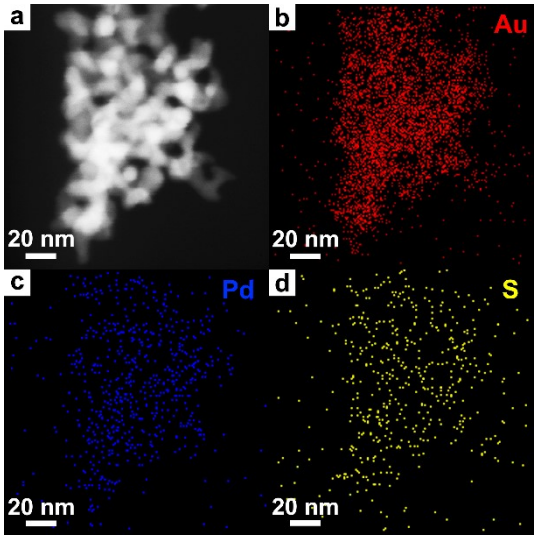

Fig. S31 Chronoamperometric (CA) curves of commercial Pt/C catalysts (a), AuPd-$S_{B_{67}A_{33}}$ aerogels (b) and AuPd-$S_{B_{50}A_{50}}$ aerogels (c), which were carried out at 0.7 V (vs RHE) in O_2-saturated 0.1 M KOH solution at a rotation speed of 1600 rpm.

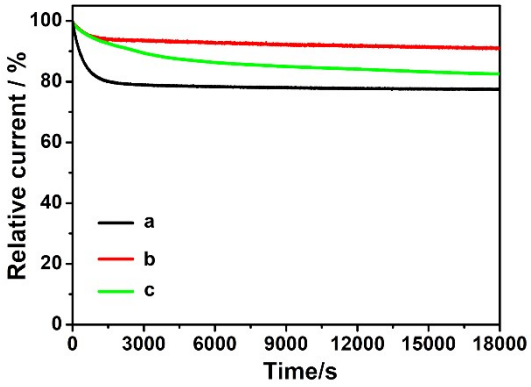

Table S1 Summarized data of the ratios of Pd(0) and Pd(II) in AuPd-$S_{B_{100}A_0}$ aerogels, AuPd-$S_{B_{67}A_{33}}$ aerogels and AuPd-$S_{B_{50}A_{50}}$ aerogels. These data were obtained by combined analysis of XPS and EDS data.

Samples	Pd(0)	Pd(II)	
	Pd [%]	PdS_2 [%]	$Pd_{2.8}S$ [%]
AuPd-$S_{B_{100}A_0}$ aerogels	40.82	59.18	-
AuPd-$S_{B_{67}A_{33}}$ aerogels	44.78	36.12	19.10
AuPd-$S_{B_{50}A_{50}}$ aerogels	58.87	19.28	21.85

Table S2 Comparison in electrocatalytic performance of our samples (AuPd-$S_{B_{67}A_{33}}$ aerogels and AuPd-$S_{B_{50}A_{50}}$ aerogels) and other Pd-based electrocatalysts towards to ORR in 0.1 M KOH solution.

Sample	E_{onset} [V]	$E_{1/2}$ [V]	$E_{1/2}$ of Pt/C [V]	$\Delta E_{1/2}$ [mV]	Reference
AuPd-$S_{B_{67}A_{33}}$ aerogels	1.067	0.970	0.885	85	This work
AuPd-$S_{B_{50}A_{50}}$ aerogels	1.056	0.950	0.885	65	This work
RuO_x-on-Pd NSs/C		0.93	0.86	70	Angew. Chem. Int. Ed. 2021, 60, 16093–16100.[30]
2H-$Pd_{67}Cu_{33}$ NPs	-	0.905	0.845	60	J. Am. Chem. Soc. 2021,143, 17292–17299.[31]
2H-$Pd_{71}Cu_{22}Pt_7$	-	0.927	0.845	82	J. Am. Chem. Soc. 2021,143, 17292–17299.[31]
Pd/N–HsGY	0.96	0.849	0.827	22	J. Mater. Chem. A, 2021, 9, 14507–14514.[32]
$Pd_{17}Se_{15}$ NPs/C	-	~0.91	-	-	Nano Lett. 2021, 21, 3805−3812.[33]
PdBi_8h	1.0	~0.92	~0.92	~0	ACS Catal. 2021, 11, 800−808.[34]
Pd/NRGO in situ (32% loading)	1.06	0.93	0.86	70	J. Mater. Chem. A 2021, 9, 10966−10978.[35]
$Pd_{31}Bi_{12}$/C	0.97	0.92	0.87	50	ACS Energy Lett. 2020, 5, 17−22.[36]
Pd_4Au HCs/C	-	0.87	0.85	20	Adv. Energy Mater. 2020, 10, 1904072.[37]
Pd@PdFe core−shell icosahedra/C	-	~0.9	-	-	Nano Lett. 2020, 20, 1403−1409.[38]
Pd_3Au/C	0.988	0.866	0.846	23	Appl. Catal., B 2020, 262. 118298.[39]
h-BN/C/Pd:17	-	0.91	Pd/C-0.9		Nano Lett. 2020, 20, 6807−6814.[40]
o-Pd_2Sn/C NSs	-	0.893	0.85	43	J. Mater. Chem. A 2020, 8, 15665–15669.[41]
VW Au@Pd HNWs	1.07	0.91	Pd/C-0.85		J. Mater. Chem. A 2020, 8, 19300–19308.[42]

Table S3 Summarized data of the elemental composition of AuPd-S_{B67A33} aerogels determined by EDS before and after the ADT testing.

Samples	Au [%]	Pd [%]	S [%]
Before ADT test	82.16	11.65	6.19
After ADT test[a]	83.04	11.06	5.90
After ADT test[b]	82.16	10.94	5.84
Loss of each element before and after ADT test	0	0.71	0.35

[a] The original composition of each element; [b] The normalized composition of each element.

Given the stability of Au during the ADT testing as well as its high content, the content of Au may stay unchanged before and after the ADT testing. Therefore, the content of Au in the AuPd-S_{B67A33} aerogels before and after ADT test is used as the reference to normalize the contents of other elements. As shown in Table S3, the contents of Pd and S in the AuPd-S_{B67A33} aerogels after ADT testing are reduced from 11.65 to 10.94 %, and from 6.19 to 5.84 %, respectively. One can clearly see that only about 0.71 % of Pd and 0.35 % of S in the AuPd-S_{B67A33} aerogels are lost after their ADT testing, respectively. Therefore, the percentages of Pd loss and S loss during the ORR are rather ultra-low. Accordingly, the maximum retention of elemental Pd in the AuPd-S_{B67A33} aerogels render them have a better durability.

Table S4 Summarized data of the elemental composition determined by EDS of AuPd-$S_{B_{100}A_0}$ aerogels, AuPd-$S_{B_{67}A_{33}}$ aerogels and AuPd-$S_{B_{50}A_{50}}$ aerogels.

Samples	Au/%	Pd/%	S/%
AuPd-$S_{B_{100}A_0}$ aerogels	78.10	12.46	9.44
AuPd-$S_{B_{67}A_{33}}$ aerogels	82.16	11.65	6.19
AuPd-$S_{B_{50}A_{50}}$ aerogels	82.44	12.82	4.74

References

1. X. Zhang, S. Wang, C. Wu, H. Li, Y. Cao, S. Li and H. Xia, *J. Mater. Chem. A*, 2020, **8**, 23906-23918.
2. X. Liu, J. Xu, X. Xie, Z. Ma, T. Zheng, L. Wu, B. Li and W. Li, *Chem. Commun.*, 2020, **56**, 11034-11037.
3. Z. Ke, Z. Yu and Q. Huang, *Plasma Process. Polym.*, 2013, **10**, 181-188.
4. J. Marcelo Arias, M. E. Tuttolomondo, S. B. Diaz and A. Ben Altabef, *J. Raman Spectrosc.*, 2015, **46**, 369-376.
5. S. Rahimnejad, J. H. He, W. Chen, K. Wu and G. Q. Xu, *RSC Adv.*, 2014, **4**, 62423-62429.
6. M. A. Peck and M. A. Langell, *Chem. Mater.*, 2012, **24**, 4483-4490.
7. H. Liu, J. Li, L. Wang, Y. Tang, B. Y. Xia and Y. Chen, *Nano Res.*, 2017, **10**, 3324-3332.
8. W. Jiao, C. Chen, W. You, X. Zhao, J. Zhang, Y. Feng, P. Wang and R. Che, *Adv. Energy Mater.*, 2020, **10**, 1904072.
9. X.-K. Wan, H. B. Wu, B. Y. Guan, D. Luan and X. W. Lou, *Adv. Mater.*, 2020, **32**, 1901349.
10. F.-M. Li, Y.-Q. Kang, R.-L. Peng, S.-N. Li, B.-Y. Xia, Z.-H. Liu and Y. Chen, *J. Mater. Chem. A*, 2016, **4**, 12020-12024.
11. Q. Wang, F. Chen, L. Guo, T. Jin, H. Liu, X. Wang, X. Gong and Y. Liu, *J. Mater. Chem. A*, 2019, **7**, 16122-16135.
12. T. Tran Van, S. G. Kang, M. H. Kim, S. G. Lee, S. H. Hur, J. S. Chung and W. M. Choi, *Adv. Energy Mater.*, 2019, **9**, 1900945.
13. W. Zhang, Z. Hu, C. Fan, Z. Liu, S. Han and J. Liu, *ACS Appl. Mater. Interfaces*, 2021, **13**, 15190-15204.
14. S. Milliken, K. Cui, B. A. Klein, I. T. Cheong, H. Yu, V. K. Michaelis and J. G. C. Veinot, *Nanoscale*, 2021, **13**, 18281-18292.
15. Y.-X. Wang, M. Rinawati, W.-H. Huang, Y.-S. Cheng, P.-H. Lin, K.-J. Chen, L.-Y. Chang, K.-C. Ho, W.-N. Su and M.-H. Yeh, *Carbon*, 2022, **186**, 406-415.
16. E. C. Garnett, W. Liang and P. Yang, *Adv. Mater.*, 2007, **19**, 2946-2950.
17. T. T. Vo Doan, J. Wang, K. C. Poon, D. C. L. Tan, B. Khezri, R. D. Webster, H. Su and H. Sato, *Angew. Chem., Int. Ed.*, 2016, **55**, 6842-6847.
18. G. Guan, J. Deng, J. Ren, Z. Pan, W. Zhuang, S. He, B. Wang, R. Che and H. Peng, *J. Mater. Chem. A*, 2017, **5**, 22125-22130.
19. R. Zhou, Y. Zheng, M. Jaroniec and S.-Z. Qiao, *ACS Catal.*, 2016, **6**, 4720-4728.
20. L. Lai, J. R. Potts, D. Zhan, L. Wang, C. K. Poh, C. Tang, H. Gong, Z. Shen, J. Lin and R. S. Ruoff, *Energy Environ. Sci.*, 2012, **5**, 7936-7942.
21. C. Cao, L. Wei, M. Su, G. Wang and J. Shen, *J. Mater. Chem. A*, 2016, **4**, 9303-9310.
22. B. Mukherjee, *J. Electrochem. Soc.*, 2020, **167**, 116501.
23. L. Huo, B. Liu, G. Zhang, R. Si, J. Liu and J. Zhang, *J. Mater. Chem. A*, 2017, **5**, 4868-4878.
24. Z. Yuanjian, K. Fugane, T. Mori, N. Li and Y. Jinhua, *J. Mater. Chem.*, 2012, **22**, 6575-6580.
25. S. Knani, L. Chirchi, W. T. Napporn, S. Baranton, J. M. Leger and A. Ghorbel, *J.*

Electroanal. Chem., 2015, **738**, 145-153.
26. Y. Cong, I. T. McCrum, X. Gao, Y. Lv, S. Miao, Z. Shao, B. Yi, H. Yu, M. J. Janik and Y. Song, *J. Mater. Chem. A*, 2019, **7**, 3161-3169.
27. M. Ren, J. Chen, Y. Li, H. Zhang, Z. Zou, X. Li and H. Yang, *J. Power Sources*, 2014, **246**, 32-38.
28. H. Lu, Y. Fan, P. Huang and D. Xu, *J. Power Sources*, 2012, **215**, 48-52.
29. M. Zhao, H. Liu, H. Zhang, W. Chen, H. Sun, Z. Wang, B. Zhang, L. Song, Y. Yang, C. Ma, Y. Han and W. Huang, *Energy Environ. Sci.*, 2021, **14**, 6455-6463.
30. Z. Lyu, X.-G. Zhang, Y. Wang, K. Liu, C. Qiu, X. Liao, W. Yang, Z. Xie and S. Xie, *Angew. Chem., Int. Ed.*, 2021, **60**, 16093-16100.
31. Y. Ge, X. Wang, B. Huang, Z. Huang, B. Chen, C. Ling, J. Liu, G. Liu, J. Zhang, G. Wang, Y. Chen, L. Li, L. Liao, L. Wang, Q. Yun, Z. Lai, S. Lu, Q. Luo, J. Wang, Z. Zheng and H. Zhang, *J. Am. Chem. Soc.*, 2021, **143**, 17292-17299.
32. W. Si, Z. Yang, X. Hu, Q. Lv, X. Li, F. Zhao, J. He and C. Huang, *J. Mater. Chem. A*, 2021, **9**, 14507-14514.
33. Z. Yu, S. Xu, Y. Feng, C. Yang, Q. Yao, Q. Shao, Y.-f. Li and X. Huang, *Nano Lett.*, 2021, **21**, 3805-3812.
34. S. Sarkar, S. D. Ramarao, T. Das, R. Das, C. P. Vinod, S. Chakraborty and S. C. Peter, *ACS Catal.*, 2021, **11**, 800-808.
35. L. Sahoo, S. Mondal, A. Gloskovskii, A. Chutia and U. K. Gautam, *J. Mater. Chem. A*, 2021, **9**, 10966-10978.
36. Y. Wang and A. S. Hall, *ACS Energy Lett.*, 2020, **5**, 17-22.
37. W. Jiao, C. Chen, W. You, X. Zhao, J. Zhang, Y. Feng, P. Wang and R. Che, *Adv. Energy Mater.*, 2020, **10**, 1904072.
38. X. Li, X. Li, C. Liu, H. Huang, P. Gao, F. Ahmad, L. Luo, Y. Ye, Z. Geng, G. Wang, R. Si, C. Ma, J. Yang and J. Zeng, *Nano Lett.*, 2020, **20**, 1403-1409.
39. W. Jiao, C. Chen, W. You, G. Chen, S. Xue, J. Zhang, J. Liu, Y. Feng, P. Wang, Y. Wang, H. Wen and R. Che, *Appl.Catal., B*, 2020, **262**, 118298.
40. Y. Chen, J. Cai, P. Li, G. Zhao, G. Wang, Y. Jiang, J. Chen, S. X. Dou, H. Pan and W. Sun, *Nano Lett.*, 2020, **20**, 6807-6814.
41. J. Liang, S. Li, Y. Chen, X. Liu, T. Wang, J. Han, S. Jiao, R. Cao and Q. Li, *J. Mater. Chem. A*, 2020, **8**, 15665-15669.
42. J. Wang, X. Qiu, K. Su, S. Wang, J. Li and Y. Tang, *J. Mater. Chem. A*, 2020, **8**, 19300-19308.